

Lawrence Berkeley National Laboratory

LBL Publications

Title

Coordinated JWST Imaging of Three Distance Indicators in a Supernova Host Galaxy and an Estimate of the Tip of the Red Giant Branch Color Dependence

Permalink

<https://escholarship.org/uc/item/9ws3213p>

Journal

The Astrophysical Journal, 975(1)

ISSN

0004-637X

Authors

Hoyt, Taylor J
Jang, In Sung
Freedman, Wendy L
[et al.](#)

Publication Date

2024-11-01

DOI

10.3847/1538-4357/ad7952

Copyright Information

This work is made available under the terms of a Creative Commons Attribution License, available at <https://creativecommons.org/licenses/by/4.0/>

Peer reviewed



Coordinated JWST Imaging of Three Distance Indicators in a Supernova Host Galaxy and an Estimate of the Tip of the Red Giant Branch Color Dependence

Taylor J. Hoyt¹ , In Sung Jang² , Wendy L. Freedman³ , Barry F. Madore^{2,4} , Abigail J. Lee² , and Kayla A. Owens² ¹ Physics Division, Lawrence Berkeley National Lab, 1 Cyclotron Road, Berkeley, CA 94720, USA; taylorjhoyt@gmail.com² Department of Astronomy & Astrophysics, University of Chicago, 5640 South Ellis Avenue, Chicago, IL 60637, USA³ Department of Astronomy & Astrophysics and Kavli Institute for Cosmological Physics, University of Chicago, 5640 South Ellis Avenue, Chicago, IL 60637, USA⁴ The Observatories of the Carnegie Institute of Washington, 813 Santa Barbara St, Pasadena, CA 91101, USA

Received 2023 September 18; revised 2024 July 9; accepted 2024 September 9; published 2024 October 29

Abstract

Boasting a 6.5 m mirror in space, JWST can increase by several times the number of supernovae (SNe) to which a redshift-independent distance has been measured with a precision distance indicator (e.g., tip of the red giant branch (TRGB) or Cepheids); the limited number of such SN calibrators currently dominates the uncertainty budget in distance ladder Hubble constant (H_0) experiments. JWST/NIRCAM imaging of the Virgo Cluster galaxy NGC 4536 is used here to preview JWST program GO-1995, which aims to measure H_0 using three stellar distance indicators (Cepheids, TRGB, and J-branch asymptotic giant branch/carbon stars). Each population of distance indicator was here successfully detected—with sufficiently large number statistics, well-measured fluxes, and characteristic distributions consistent with ingoing expectations—so as to confirm that we can acquire distances from each method precise to about 0.05 mag (statistical uncertainty only). We leverage overlapping Hubble Space Telescope imaging to identify TRGB stars, crossmatch them with the JWST photometry, and present a preliminary constraint on the slope of the TRGB’s F115W versus (F115W – F444W) relation equal to -0.99 ± 0.16 mag mag⁻¹. This slope is consistent with prior slope measurements in the similar Two Micron All-Sky Survey J band, as well as with predictions from the BaSTI isochrone suite. We use the new TRGB slope estimate to flatten the 2D TRGB feature and measure a (blinded) TRGB distance relative to a set of fiducial TRGB colors, intended to represent the absolute fiducial calibrations expected from geometric anchors such as NGC 4258 and the Magellanic Clouds. In doing so, we empirically demonstrate that the TRGB can be used as a standardizable candle at the IR wavelengths accessible with JWST.

Unified Astronomy Thesaurus concepts: Distance indicators (394); James Webb Space Telescope (2291); Galaxy stellar content (621)

1. Introduction

The trajectory of paradigm-shifting improvements in the realm of extragalactic distance measurement is closely tied to similar breakthroughs in observational capabilities. From the initial discovery of the expanding Universe made possible by the 100" telescope at Mount Wilson (E. Hubble 1929), to the adoption of red-sensitive plates (e.g., W. Baade 1944), the development of CCD cameras (e.g., J. Mould & J. Kristian 1986; W. L. Freedman 1988; W. L. Freedman & B. F. Madore 1988), and the launch of space telescopes (e.g., W. L. Freedman et al. 2001; A. G. Riess et al. 2009; W. L. Freedman et al. 2012; A. G. Riess et al. 2016, 2022). Now, JWST has been successfully launched, commissioned, and is in full science operation (J. P. Gardner et al. 2023; J. Rigby et al. 2023). With a 6.5 m mirror diameter and newer IR detector technology than its predecessors, JWST has already begun rapidly improving the precision and accuracy of extragalactic distance measurements (G. S. Anand et al. 2024; A. J. Lee et al. 2024a; A. G. Riess et al. 2024).

1.1. The Hubble Constant

The Universe’s present-day expansion rate, or the Hubble constant, H_0 , continues to prove challenging to accurately

measure via direct, astrophysical means such as the classical distance ladder. After the Key Project resolved the factor of 2 debate using the Hubble Space Telescope (HST) and introduced comprehensive error budgeting into the distance scale (W. L. Freedman et al. 2001), interest in measurement of H_0 was reignited because of the leverage it provides in constraining the dark energy equation of state when combined with cosmic microwave background (CMB) measurements (W. Hu 2005).

A departure from this initial goal of measuring w began with claims of a “Hubble Tension,” which is a disagreement between local or direct measurements of H_0 (e.g., Cepheids and supernovae (SNe)) and those estimates that are tied to high-redshift observables (e.g., CMB or Big Bang nucleosynthesis + baryon acoustic oscillations) then extrapolated to the present day. The latest evidence from Cepheids and SNe suggests that the Hubble Tension has reached 5σ significance (A. G. Riess et al. 2022) and that new physics beyond the standard model must be the reason for it. However, the Cepheid–SN local measurement dominating the claim (A. G. Riess et al. 2022) may not fully account for some uncertainties that were demonstrated to have been previously underestimated (W. L. Freedman & B. F. Madore 2023).

1.2. JWST GO-1995: Is the Tension in the Hubble Constant Real?

To address the nature of the Hubble Tension, a JWST program (PI: Freedman, co-PI: Madore, GO-1995) aims to



Original content from this work may be used under the terms of the [Creative Commons Attribution 4.0 licence](https://creativecommons.org/licenses/by/4.0/). Any further distribution of this work must maintain attribution to the author(s) and the title of the work, journal citation and DOI.

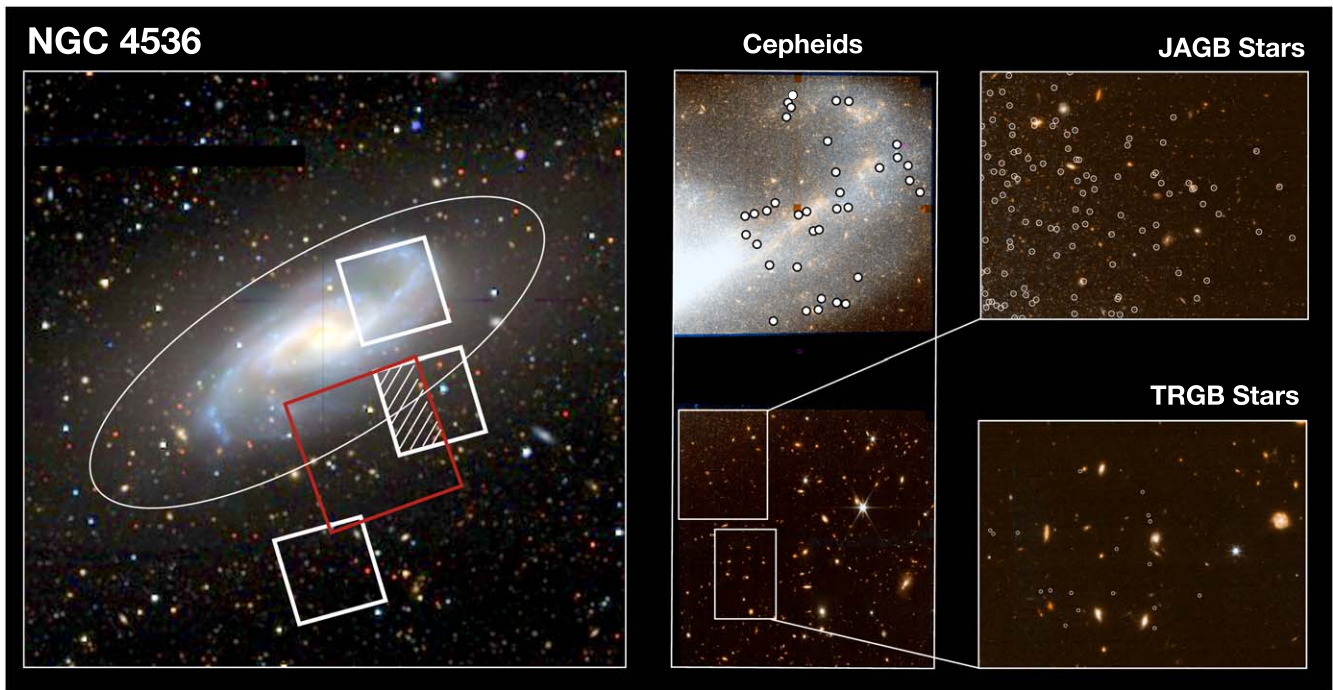


Figure 1. The successful imaging and detection of three stellar distance indicators in NGC 4536. Left: DECaLS *gri* image. Footprints of the JWST/NIRCam (pair of white squares), NIRISS (singular white square), and archival HST/Advanced Camera for Surveys (ACS; red square) imaging are plotted, with the overlap of the JWST and HST imaging marked (white hatched). North is up, east is left. The outer region of the galaxy adopted for TRGB analysis lies outside the indicated elliptical radius (white ellipse) of the galaxy’s disk ($b/a = 0.36$, $\theta = 120.^\circ 7$), which is adopted from HyperLEDA (D. Makarov et al. 2014) (<http://leda.univ-lyon1.fr/>) and corresponds to a distance along its semimajor axis (SMA) equal to 7.5 . Middle column: JWST/NIRCAM color image (Red: F444W, green: (F115W + F444W)/2, and blue: F115W). NIRCam module A is aimed at the spiral arm where H II regions are apparent and the locations of Cepheid variables from A. G. Riess et al. (2016, 2022) are overplotted (white dots with black outline). In the other NIRCam module, plentiful, highly reddened galaxies are seen in the background. Two regions are highlighted (white rectangles) to emphasize where each of the JAGB and TRGB stars are well measured, respectively. Right: zoomed views of the two rectangular regions. The carbon-enhanced JAGB stars (top rectangle) appear red and are clearly distinguished from the RGB stars, which appear blue (relative to $4.4 \mu\text{m}$). The JAGB stellar density also falls off more quickly in radial distance than that of the RGB’s due to the galaxy’s outer disk profile being steeper than that of its stellar halo.

assess how well the facility can measure extragalactic distances by comparing relative distances estimated to the same host galaxies using three different distance indicators. The program is designed to acquire JWST/NIRCAM imaging of 10 galaxies that have hosted Type Ia supernovae (SNe Ia) as well as of three fields in the megamaser host galaxy NGC 4258, to which a 1.5% trigonometric distance has been estimated (J. R. Herrnstein et al. 1999; E. M. L. Humphreys et al. 2008, 2013; M. J. Reid et al. 2019). These calibrator galaxies play the key role as the absolute anchors of the SN Ia distance scale, and any subsequent SN-based derivation of H_0 .

In each pointing, imaging was acquired so as to capture at the same time three distance indicators: the classical Cepheid variables, the tip of the red giant branch (TRGB), and the predominantly carbon-enhanced population of red asymptotic giant branch (AGB) stars that are found to populate a horizontal plume in the J -band color–magnitude diagram (CMD), referred to as JAGB. Each of the three methods can be naturally categorized by the galactic structures in which their respective stellar populations are optimally measured: the young, massive Cepheids in spiral arms and/or thin disks, intermediate-age JAGB stars in the thick, extended disk, and the old TRGB in the stellar halo (see Figure 1).

The program was blinded in terms of both the intrasample relative distances as well as the sample-wide absolute zero-point. This is done by injecting a random offset, different for each of the 13 target fields, between -0.2 and $+0.2$ mag into

each field’s photometric catalog, then deleting all traces of the original magnitudes. After unblinding, each method’s calibrated distance scale will provide a new measure of the Hubble constant and, should the cross comparison reveal minimal systematic differences, the joint distance constraints can be leveraged for a combined determination of the Hubble constant with improved uncertainties over any one method’s constraint.

In this paper, each of the three methods will be showcased using JWST/NIRCAM observations acquired of the Virgo Cluster galaxy NGC 4536—with an outsize focus placed on the TRGB and its color dependence. We briefly introduce each method here and emphasize recent developments relevant to the IR imaging considered here. For a comprehensive review of each method and of the motivation for program JWST GO-1995, see W. L. Freedman & B. F. Madore (2023).

1.3. Cepheid Variable Stars

Cepheid variables have long been the backbone of modern observational cosmology via application of the “Leavitt Law,” or the universal power-law relationship between a Cepheid’s pulsation period and its phase-averaged luminosity (H. S. Leavitt 1908; H. S. Leavitt & E. C. Pickering 1912). The Cepheid Leavitt Law was used to discover the expanding Universe (E. Hubble 1929), and then revised via disambiguation between the classical and Population II Cepheids, which populate separate period–luminosity relations (PLRs; W. Baade & H. H. Swope 1963). It underpinned the factor of 2 debate over

the age of the Universe (see, e.g., A. R. Sandage 1970; G. de Vaucouleurs 1978), as well as its resolution, which began with some of the earliest observations of Cepheids with CCDs (e.g., W. L. Freedman 1988; W. L. Freedman & B. F. Madore 1990) and finished with the HST Key Project (HST-KP; W. L. Freedman et al. 2001).

The HST-KP techniques were further developed and broadened in scope for use with near-infrared (NIR) detectors on board HST such as NICMOS (L. M. Macri et al. 2001; A. G. Riess et al. 2009) and WFC3/IR (A. G. Riess et al. 2016, 2022). With Spitzer, extinction uncertainties could be reduced to negligible levels (W. L. Freedman et al. 2012). This led to the discovery of a bandpass ($\lambda_{\text{eff}} = 4.5 \mu\text{m}$) in which a CO band-head could be observed and provide a means of acquiring direct abundance measurements of Cepheids from photometry alone (V. Scowcroft et al. 2011; A. J. Monson et al. 2012; V. Scowcroft et al. 2016), at nearly the same precision as spectroscopy ($\sigma \simeq 0.2$ dex). The CO band-head has recently been directly confirmed with spectroscopic measurements of Cepheids (S. L. Hamer et al. 2023).

JWST can directly build on the pioneering findings provided by Spitzer, which was limited to the nearby ~ 100 kpc Universe. JWST increases the reach of $4.5 \mu\text{m}$ Cepheid measurements to the 10 Mpc Universe and potentially beyond, thanks to its considerably better image quality—predominantly a function of the 8 times increase in mirror size, though newer generation IR imaging technology also plays a major role. The measurement of Cepheid fluxes at $4.5 \mu\text{m}$ and the potential to directly measure Cepheid metallicities was considered in planning the JWST GO-1995 observations of the most nearby targets (e.g., M101 and NGC 4258). For the remainder of the targets we chose to pair F115W with the F356W $3.6 \mu\text{m}$ band as it is the most sensitive of the NIRCAM/long wavelength (LW) standard wide bandpasses. This excludes NGC 4536 and NGC 7250, which were imaged in F444W before we made the decision to switch to F356W for distant targets.

1.4. Horizontal J Branch of Carbon-enhanced Asymptotic Giant Branch Stars

Two Micron All-Sky Survey (2MASS) observations of the LMC revealed a distinct branch of stars pulling off the narrow oxygen-rich AGB (S. Nikolaev & M. D. Weinberg 2000). M. D. Weinberg & S. Nikolaev (2001) used that branch of stars to present a constraint on the geometry of the LMC that was consistent with prior determinations derived from established distance indicators (e.g., Cepheids), demonstrating that this branch of AGB stars was capable of providing precise distances when observed in the IR.

B. F. Madore & W. L. Freedman (2020a) updated the M. D. Weinberg & S. Nikolaev (2001) findings by identifying from an expansive compilation of IR CMDs of the LMC (L. M. Macri et al. 2015; T. J. Hoyt et al. 2018) that this branch of AGB stars became almost completely horizontal when observed in a *J*-band CMD. P. Ripoche et al. (2020) found the same in 2MASS observations of the LMC and IR observations plus Gaia Data Release 2 parallaxes of Milky Way stars. W. L. Freedman & B. F. Madore (2020) used this JAGB method to determine distances to 13 Local Group galaxies, comparing against the *I*-band TRGB and finding a total dispersion of 0.07 mag, thereby establishing the JAGB as a precision distance indicator. The method has been vetted and refined upon by several independent groups, across different

host galaxies, and tested with various approaches to the actual distance measurement methodology (A. J. Lee et al. 2021; J. Parada et al. 2021, 2023; B. Zgirski et al. 2021; A. J. Lee et al. 2024b).

1.5. The Tip of the Red Giant Branch

When observed at the NIR wavelengths at which a TRGB star’s spectral energy distribution peaks, the TRGB brightness is strongly (and linearly) correlated with the metallicities/colors of coeval TRGB stars (M. Salaris & S. Cassisi 1998; M. Bellazzini et al. 2004; M. Salaris & S. Cassisi 2005; M. Bellazzini 2008; B. F. Madore et al. 2018; M. J. Durbin et al. 2020; B. F. Madore & W. L. Freedman 2020b), contrary to its metallicity/color-insensitive (with a small, near-zero residual variance observed for metal-poor TRGB stars) manifestation when observed with bands that have effective wavelengths between 800 and 900 nm (M. G. Lee et al. 1993; M. Bellazzini et al. 2001; I. S. Jang & M. G. Lee 2017; K. B. W. McQuinn et al. 2019; W. L. Freedman 2021; T. J. Hoyt 2023; G. S. Anand et al. 2024). As a result, calibration of the TRGB’s color dependence becomes the most important step to measuring precise and accurate TRGB distances in the NIR.

There is general consensus in the literature that the shape of the NIR TRGB’s color dependence is linear (E. Valenti et al. 2004; M. Bellazzini 2008; A. Serenelli et al. 2017; B. F. Madore et al. 2018; M. J. Durbin et al. 2020).⁵ However, at times, significant discrepancies in empirical zero-points larger than 0.2 mag have been reported (E. Valenti et al. 2004; M. Górski et al. 2016).⁶

In a joint study of IC 1613 and the LMC, B. F. Madore et al. (2018) and T. J. Hoyt et al. (2018) painted an optimistic picture for use of the TRGB in the NIR. They determined a TRGB color slope in IC 1613 and subsequently used it to construct a high-precision map of the apparent line-of-sight depth of the LMC. In doing so, they confirmed the LMC’s known NE–SW tilt with a field-to-field residual distance dispersion of ~ 0.05 mag. A similarly positive outlook was presented in K. B. W. McQuinn et al. (2019) who presented TRGB magnitudes that were synthesized by passing PARSEC isochrone predictions through anticipated JWST filter curves.

Both of these prior studies emphasized that the NIR TRGB can be a precision distance indicator as long as a robust fiducial calibration of its variation with color is determined; the variation with color is primarily a metallicity and secondarily an age effect. In this study, we will report the successful detection of the NIR TRGB feature with JWST and demonstrate that we can measure its color dependence. We then demonstrate how the use of such a color correction can significantly improve both the accuracy and precision of a TRGB distance.

In Section 2, we describe the observation planning of the JWST program, the reduction of the NGC 4536 images, and the sample selection procedure. In Section 3, we present the successful detection of all three distance indicators. In Section 4, we estimate the TRGB’s color dependence in the

⁵ Though see P.-F. Wu et al. (2014), who presented evidence of two distinct slopes in the blue and red color regimes, i.e., two slopes with a break, for the HST F110W and F160W bands, which may be a genuinely anomalous effect for those bands (A. Serenelli et al. 2017).

⁶ See T. J. Hoyt et al. (2018) and T. J. Hoyt (2023) for resolutions to some of these discrepancies.

F115W band, use it to estimate the TRGB’s color-corrected magnitude, then test an expanded range of slope values on the data. We discuss the results in Section 5 and conclude in Section 6.

2. Observations and Data

2.1. Configuring the Program Observations

As mentioned, JWST program GO-1995 aims to measure three different stellar distance indicators—Cepheids, TRGB, and JAGB—simultaneously from one set of imaging per target. Accomplishing this imposed constraints on the placement of the scientific apertures, as well as on the allowed rotation angles of the telescope.

For each target, the offset values of the NIRC*am* aperture were set so as to minimize loss of Cepheid coverage over large ranges of allowed telescope rotation angles, thereby maximizing schedulability at a minimal science loss. For observing the JAGB stars, additional constraints on the telescope’s commanded position angles were determined using deep ground-based imaging from the DECALS legacy imaging survey (A. Dey et al. 2019), as well as HI maps of the target galaxies when available. The goal was to sample each galaxy’s thick disk component while minimizing the likelihood of dust extinction systematically biasing a JAGB measurement. Finally, (T)RGB stars were either targeted with (some portion of) the module of NIRC*am* that was not aimed at the Cepheids or with parallel NIRISS observations, depending on the angular extent of the target galaxy. In some cases, there existed ACS/Wide Field Channel (WFC) observations of the TRGB from the Carnegie Chicago Hubble Program (W. L. Freedman et al. 2019). Sampling some portion of those image sets was taken into consideration in order to leverage both optical and NIR photometry and better understand the TRGB magnitude–color relation (as in the present study).

JWST has complex, observatory-wide constraints that limit certain configuration parameters (e.g., absolute limits on the roll angle of the telescope given a target’s position on the sky). In a small number of the program observations, this forced nonoptimal configurations that, fortunately, did not significantly impact the science. Typical examples include the dropout of one or a few Cepheid variables, or a reduced overlap with archival HST imaging. It is our recommendation that future investigators anticipate their exact roll angle requirements as accurately and early as possible when planning a program so as to avoid having to make unanticipated trade-offs in the Phase 2 implementation.

2.2. Image Processing and Photometry

We downloaded from MAST the 90 NIRC*am* integrations of our field in NGC 4536 (Figure 1). The JWST image set is composed of nine dithers mapped to each of the 10 NIRC*am* detectors: eight in the short wavelength (SW) and two in the LW channels. Each integration was composed of six groups, resulting in an effective exposure time of 2802.297 s in the F115W (SW) and F444W (LW) bands acquired at one epoch of the imaged Cepheids’ light curves.

We processed the image data from raw to calibrated cal and undistorted i2d images using the `jwst` module version v1.8.2. The JWST calibration pipeline version number is implicitly associated with a set of calibration reference files such as the reference dark and flat images, among other image processing

and calibration information. Two independent processing scripts, one from the command line and one in Jupyter Notebook, were implemented with default settings and confirmed to match exactly the MAST data products from the automated STScI processing pipeline.

The aligned F115W and F444W cal images were then photometered with the DOLPHOT NIRC*am* module (D. R. Weisz et al. 2023, 2024) that was developed as part of the JWST Early Release Science program on Stellar Populations (PI: Weisz). At the time of the present analysis, the JWST DOLPHOT module was not fully released, and we used a beta early release version that was graciously provided by the JWST GO-1334 ERS team (PI: Weisz). The version used implicitly incorporated the critical updates to the NIRC*am* detector zero-points that were implemented in `pmap0989` (M. L. Boyer et al. 2022). Aperture corrections were made using the DOLPHOT routine corresponding to $ApCor = 1$.

The archival CCHP HST/WFC data (GO-13691, PI: Freedman) acquired in the F606W and F814W bands were also reduced using DOLPHOT with a custom aperture correction routine applied that is expected to be more accurate than the automated DOLPHOT routines in the case of deep HST photometry (I. S. Jang 2023).

Note that the JWST/NIRC*am* photometry used in the analysis presented here was “blinded” by injecting into the photometry catalog a random, uniformly distributed offset between -0.2 and $+0.2$ mag, so the absolute flux zero-points of NIRC*am* do not play a role. Only the relative intramodule, detector-to-detector calibration would impact our analysis, and the post-`pmap0989` detector-to-detector zero-point uncertainties are at or below the measurement uncertainties discussed here. This is because any shifts to the absolute photometric zero-points, the dominant uncertainty in the ongoing JWST flux calibration, amount to translations on the CMD, thereby not distorting the TRGB morphology, i.e., its slope with color.

Both HST and JWST catalogs were trimmed for well-measured point sources as described in I. S. Jang (2023). The two catalogs were then crossmatched in the world coordinate system (WCS) with a $0''.12$ radius threshold using methods from the `astropy.coordinates` module. There was an approximate $0''.05$ offset in both R.A. and decl. between the default ACS and NIRC*am* WCS solutions, with no evidence of higher order functionality in the aligned coordinate residuals. The offset corrections were applied and the matching radius reduced to $0''.08$. The final dispersion about each matched set of coordinates was $0''.01$, or <0.2 pixels for each instrument.

The photometry was extinction corrected using a foreground reddening of $E(V - I) = 0.023 \pm 0.012$ mag adopted from the E. F. Schlafly & D. P. Finkbeiner (2011) recalibration of the D. J. Schlegel et al. (1998) maps, as compiled in the NED extragalactic database.⁷ This corresponds to $A_{F606W} = 0.045$ mag, $A_{F814W} = 0.028$ mag, $A_{F115W} = 0.014$ mag, and $A_{F444W} = 0.001$ mag. An uncertainty equal to half of the reddening value is adopted due to the increased uncertainty associated with measuring Milky Way dust in regions of low column density (i.e., at high Galactic latitude).

2.3. Sample Definitions and Spatial Selections

Due to the different underlying physics, each distance indicator’s population can be found in distinct regions on both the H-R diagram and in the spatial distribution of a galaxy’s stellar mass.

⁷ <http://ned.ipac.caltech.edu>

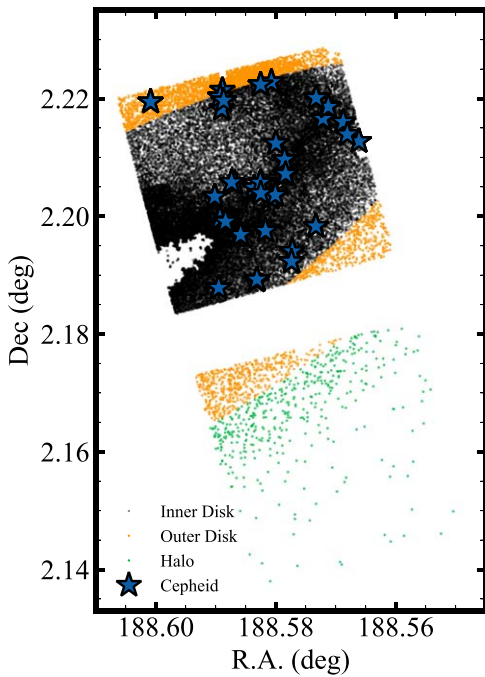


Figure 2. Sources brighter than the approximately identified TRGB magnitude (see Figure 3) are plotted as dots. The spiral arm is clearly revealed in the upper module and contained in the inner disk selection (black dots). The dearth of sources in the outermost region of the imaging (green dots) is the hallmark of an old stellar population, i.e., a spatial manifestation of the TRGB. The intermediate region is identified as the “outer disk” (orange dots). The interplay between this diagnostic and Figure 3 was used to converge on spatial selections for the JAGB and TRGB measurements.

The Cepheids are found in the star-forming spiral arms and thin disk, the JAGB in the thermally dispersed thick disk, and TRGB the diffuse stellar halo. Therefore, we can iteratively converge on an optimal spatial selection by examining the resultant CMD until each distance indicator appears most accurately measured.

This process is illustrated in Figure 2, which plots the locations of all sources in the JWST catalog that are brighter than what is estimated to be the magnitude of the TRGB (green lines in Figure 3). The spiral arm stands out as a clear overdensity amidst the black points, consistent with it containing the youngest and brightest stars. Outside of the spiral arm is a component that is slightly more diffuse and smooth in its structure, but still has a measurable number of bright stars embedded in it, i.e., an intermediate-age population. Finally, at the largest separation from the disk components we start to see a constant and negligible density of stars brighter than the TRGB, which is indicative of an old stellar population.

These three regions delineate where each of the three standard candles is best measured. Though in the case of the young, massive Cepheids, the star-forming disk and spiral arm structures of galaxies are simply the only regions in which they can be found.

The starting sample of Cepheids is the set union of those discovered and reported by two iterations of the SH0ES project (S. L. Hoffmann et al. 2016; A. G. Riess et al. 2022, hereafter H16 and R22). The periods were derived using WFPC2 observations acquired as part of the Sandage H_0 project that was conducted at the same time as the HST-KP (A. Sandage 1994; A. Saha et al. 1996). These were then followed up by the SH0ES program to place the Cepheid magnitudes onto the WFC3 system and update periods as needed (A. G. Riess et al. 2009).

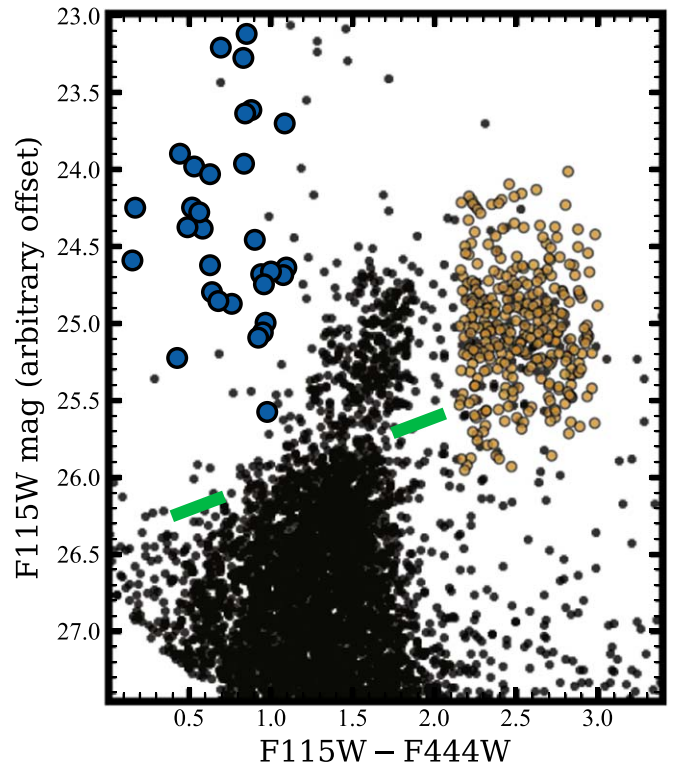


Figure 3. The simultaneous identification of three stellar distance indicators in NGC 4536 is demonstrated by overlaying three distinct stellar populations on the CMD. Black points are all stars contained in the halo selection (see Figure 2), with the green lines outlining the TRGB feature (explored in detail later). Orange points are the JAGB stars selected in the outer disk region via their colors ($F115W - F444W > 2.2$ mag). Blue points are Cepheids, which predominantly occupy the inner disk region.

We found significant shifts of $\delta R.A. = -0''.59$ and $\delta decl. = 1''.24$ had to be added to the H16 coordinates to align them with the R22 ones. The R22 coordinates were then shifted by $\delta R.A. = -0''.092$ and $\delta decl. = 0''.510$ to align them with our JWST WCS solution at a critical matching radius of $0''.08$. Doing so resulted in a sample of 35 Cepheids with periods ranging from 10 to 100 days. All 35 crossmatched Cepheids were included in H16 and 28 in R22. This particular sample of Cepheids is very well measured relative to other more crowded data sets, so the possibility for false negatives or false positives in the cross identification is very low. This can be verified via inspection of the Cepheid PLR (Figure 4). The Cepheid sample is already limited in numbers, and the number of Cepheids with well-measured F444W magnitudes was smaller yet (about 3–5), so we do not consider that band for the Cepheids here.

The other two indicators are best measured outside of the blue, star-forming regions of galaxies. See, e.g., R. L. Beaton et al. (2019), T. J. Hoyt et al. (2021b), I. S. Jang et al. (2021), and J. Wu et al. (2023) for TRGB and A. J. Lee et al. (2024a) for JAGB. Therefore, we elect to use the B -band surface brightness contours to parameterize our spatial selection, with the intent to mask the bluest star-forming regions. The adopted ellipse profile is the D_{25} B -band isophote presented in HyperLEDA, with a $b/a = 0.36$ and $\theta = 120.7$ (D. Makarov et al. 2014).⁸

⁸ <http://leda.univ-lyon1.fr/>

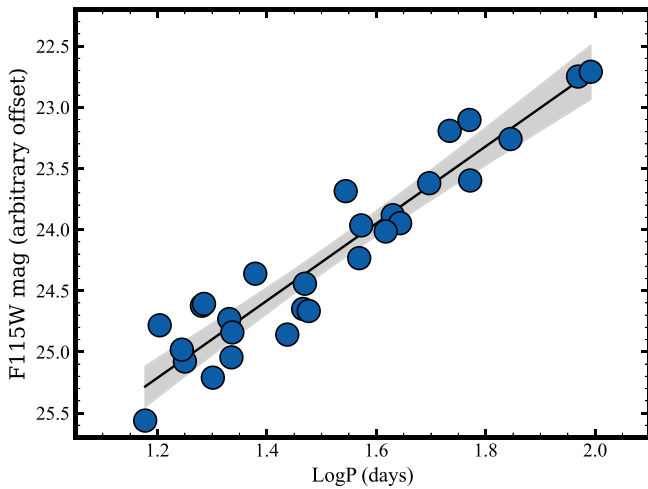


Figure 4. Cepheid PLR constructed directly from the measured F115W magnitudes and periods from the latest SH0ES sample of 28 Cepheids (R22). No correction has been applied for local scene crowding (see, e.g., A. G. Riess et al. 2016, for a description) nor for extinction. The value of the best-fit slope is -3.15 ± 0.21 mag mag $^{-1}$, and the dispersion about that slope is 0.240 ± 0.024 mag. The typical F115W photometric uncertainties are 0.015 mag and smaller than the plotted markers.

With this parameterization, we select for the JAGB an “outer disk” component at $SMA > 3'.2$ and for the TRGB an old/halo component at $SMA > 7'.5$. For the JAGB the SMA was varied until the population was clearly visible and visually distinct on the CMD (see orange dots in Figure 3). JAGB stars were then further isolated on the CMD for colors $2.2 < (F115W - F444W) < 3.0$ mag and magnitudes $24.0 < F115W < 26.0$ mag. The spatial selection is plotted as orange dots in Figure 2 and the color-selected JAGB stars as orange circles in Figure 3.

For the TRGB, a similar iterative procedure was done that instead used the visual contrast of the TRGB as observed in the overlapping HST F814W-band imaging from which the TRGB has previously been identified (W. L. Freedman et al. 2019). As can be seen from the overlay with ground-based imaging in Figure 1, the adopted halo-TRGB selection is consistent with a steep decline in diffuse light seen in the outer regions of NGC 4536, providing an unresolved consistency check on the resolved-star halo selection. The adopted halo region is marked by green dots in Figure 2 and the approximately identified TRGB bracketed by two green lines in Figure 3.

The spatial selection process is illustrated in Figure 2, which plots the locations of all sources in the JWST catalog that are brighter than what is estimated to be the magnitude of the TRGB (green lines in Figure 3). The spiral arm stands out as a clear overdensity amidst the black points, consistent with it containing the youngest and brightest stars. Outside of the spiral arm is a component that is slightly more diffuse and smooth in its structure, but still has a measurable number of bright stars embedded in it, i.e., an intermediate-age population. Finally, at the largest separation from the disk components we start to see a constant and negligible density of stars brighter than the TRGB, which is indicative of an old stellar population.

These three regions delineate where each of the three standard candles is best measured. Though in the case of the young, massive Cepheids, the star-forming disk and spiral arm structures of galaxies are simply the only regions in which they can be found.

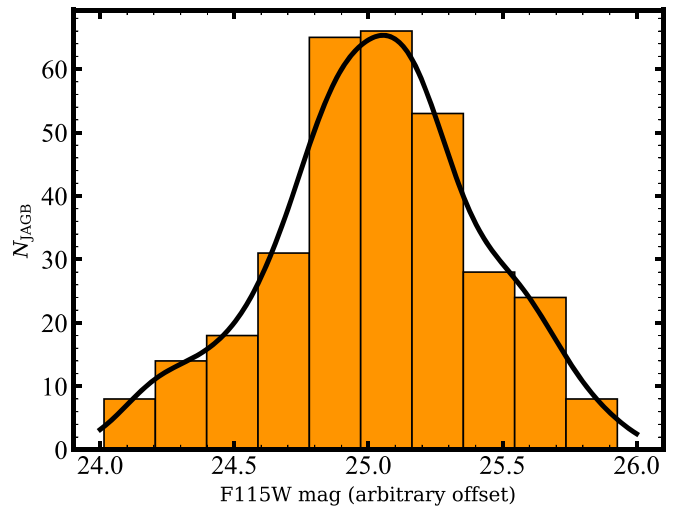


Figure 5. JAGB carbon star F115W LF, i.e., marginalizing over color for the orange points in Figure 3. The black curve is a kernel density estimate (KDE) of the distribution with modal value equal to 25.036 ± 0.056 mag.

3. Identification and Detection of Three Standard Candles

3.1. Cepheids

The Cepheid periods are zeroed to a fiducial $\log P = 1.50$ because the mean (log) period of the H16 sample is 1.48 and the mean of the R22 sample is 1.51. The slopes inferred from the H16 ($N=35$) and R22 ($N=28$) Cepheid samples are, respectively, -3.01 ± 0.19 mag mag $^{-1}$ and -3.15 ± 0.21 mag mag $^{-1}$. The corresponding intercepts are 24.239 ± 0.043 mag and 24.266 ± 0.047 mag. The dispersions about the best-fit lines are 0.246 ± 0.020 mag and 0.240 ± 0.024 mag, respectively. The 28 Cepheids in R22 are a perfect subset of the 35 in the H16 sample, so the results are highly covariant.

Note our analysis here does not include vital corrections for crowding and internal extinction (only foreground) because the evidence for both effects is near zero for this galaxy’s Cepheids (one of the most nearby and least crowded in the sample). A more complete treatment of the Cepheid PLR in these bands for the more distant Cepheids, and which supersedes this preliminary analysis, can be found in K. A. Owens et al. (2024)

The Leavitt slopes derived from either sample of Cepheids in NGC 4536 (H16 or R22) are consistent with the value of 3.15 ± 0.07 mag mag $^{-1}$ observed in the similar UKIRT/2MASS J band (separated in effective wavelength from F115W by only 90 nm). Furthermore, the measured dispersion is consistent with previous findings for random-phase sampling of Cepheids in the J band (S. E. Persson et al. 2004; A. J. Monson et al. 2012).

3.2. J -branch Asymptotic Giant Branch/Carbon Stars

In Figure 5, the JAGB luminosity function (LF) that was selected for via color and magnitude (orange disks in Figure 3) is shown. The standard deviation of the distribution is 0.381 ± 0.014 mag and the normalized median absolute deviation (NMAD) is 0.340 ± 0.025 mag. Being based on median statistics, the NMAD is more resilient to outliers and asymmetric or non-Gaussian structure in the tails of a distribution. Typical JAGB LF widths are between 0.30 mag and 0.36 mag (see, e.g., A. J. Lee et al. 2024b), confirming that we have identified the JAGB LF.

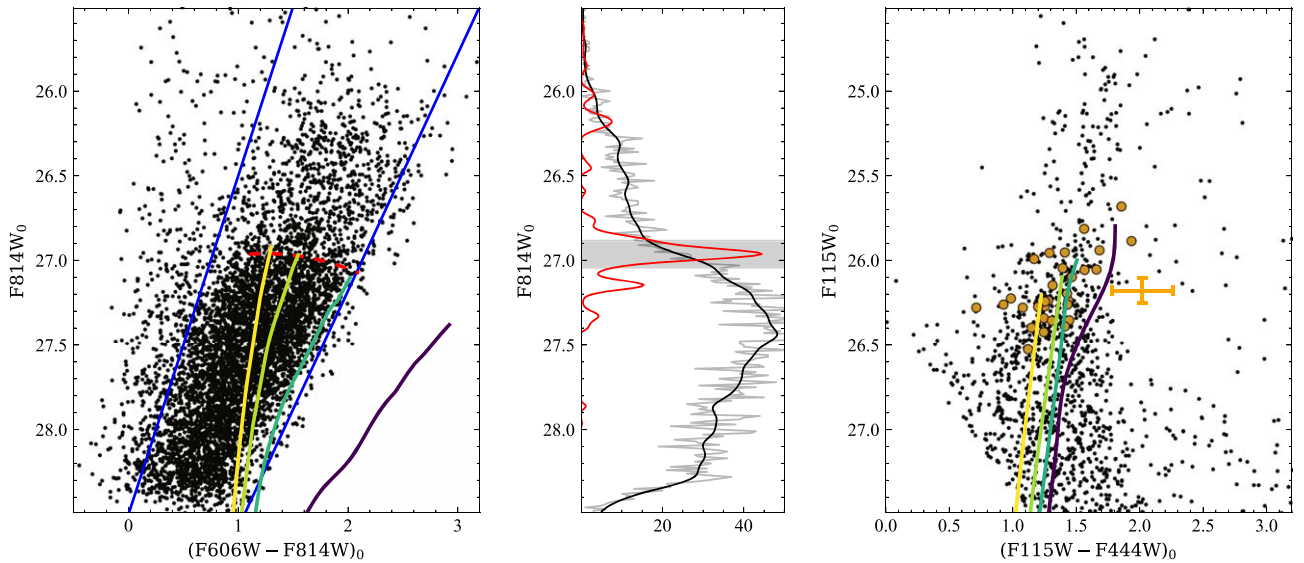


Figure 6. Identification of TRGB stars in NGC 4536 from the overlap of the optical ACS/WFC and IR NIRCcam fields of view. Left: optical CMD. The quadratic F814W band color dependence from I. S. Jang & M. G. Lee (2017) was adopted (red dashed curve) to rectify, or flatten, against color the TRGB feature contained within the selection of RGB stars (blue slanting lines). Overplotted are 10 Gyr BaSTI isochrones arbitrarily scaled along the vertical axis and colored (light yellow to dark purple) according to their metallicity $Z = \{0.002, 0.004, 0.008, Z_{\odot}\}$. Middle: the EDR (red curve) function is computed as the Poisson-weighted first derivative of the rectified LF (gray and black curve). Tip stars are identified within a ± 0.08 mag window centered on the location of the TRGB peak in the EDR. Right: the F814W-identified TRGB stars are highlighted in the JWST/NIRCAM CMD. Overplotted again are 10 Gyr BaSTI isochrones, this time as predicted for the JWST NIR filters in this study. A set of representative error bars for the TRGB stars is plotted (orange cross with caps). A single random offset between -0.2 and 0.2 mag has been applied to both of the F115W and F444W magnitudes.

To determine the JAGB magnitude, we first compute a KDE of the JAGB LF. We then resample the JAGB LF and a new modal magnitude is computed until convergence is reached in the median of the resampled modal values (found to occur at $N_{\text{resamp}} \geq 300$). The median and standard deviation of resampled modes are taken as the central value and uncertainty, respectively, resulting in an $F115W_{\text{JAGB}} = 25.036 \pm 0.056$ mag.

Our treatment of the JAGB here is superseded by the dedicated analysis from A. J. Lee et al. (2024a), which includes tests of the spatial and color selection. We do not undertake those here, and instead have simply adopted values that produce a JAGB population on the CMD that is within expectation. The aim here is not to explore the method’s uncertainties at the percent level, but to demonstrate its simplicity, that the population of stars in question have been detected in the JWST imaging, and that a precise distance can be determined.

3.3. Identifying Tip of the Red Giant Branch Stars

To identify TRGB stars in the IR CMD we look to the F814W band ($\lambda_{\text{eff}} \simeq 800$ nm) where the TRGB magnitude’s dependence on photometric color is significantly reduced relative to other wavelengths. The F814W magnitudes are rotated to a coordinate grid on which the TRGB’s (small) color dependence is ostensibly flattened (or “rectification,” as introduced in B. F. Madore et al. 2009). The specific transformation adopted here is the quadratic TRGB (QT) equation of I. S. Jang & M. G. Lee (2017), which has been shown to be most consistent with model predictions (e.g., A. Serenelli et al. 2017) and with high-precision measurements of the TRGB made in the Magellanic Clouds (T. J. Hoyt 2023). A TRGB magnitude is then measured from the QT magnitude LF according to the methodology described in T. J. Hoyt (2023) and also used by the

Carnegie Chicago Hubble Program (W. L. Freedman et al. 2019).

In Figure 6, the identification of TRGB stars is illustrated. First, as shown in the left panel of Figure 6, RGB stars are selected from the F814W and F606W CMD via a blue and red color cut (plotted as slanted blue lines). The magnitudes of these stars are then rotated to flattened QT(814) magnitudes and used to construct a new RGB LF from which the TRGB discontinuity is to be detected via computation of the Poisson-weighted first derivative, or edge detector response (EDR). The width of the TRGB peak computed from the rectified RGB LF was 15% narrower than that measured from in the unrectified RGB LF, thereby justifying the use of a color correction. For reference, BaSTI isochrones with age 10 Gyr are shown and color coded for $Z = 0.002, 0.004, 0.008$, and solar metallicity (S. L. Hidalgo et al. 2018; A. Pietrinferni et al. 2021). The curvature of the isochrone-predicted F814W TRGB agrees well with the shape of the empirical I. S. Jang & M. G. Lee (2017) QT calibration. This underscores that a second-order color correction is likely the best to use when making precise, color-corrected TRGB distances in the F814W band.

In the middle panel of Figure 6, the QT magnitude EDR is plotted as a red curve along with the F814W smoothed and unsmoothed RGB LFs as black and gray curves, respectively. A transparent, gray, horizontal band represents the window that was used to select TRGB stars within ± 0.08 mag of the peak’s location, set by the typical F814W magnitude uncertainty at the magnitude of the TRGB. Smaller and larger windows than this were tested and it was found that windows smaller than about 0.04 mag suffered from too small number statistics, and windows larger than 0.08 mag caused the TRGB slope fit to become increasingly skewed from the 2D edge feature toward tracing the steep slope of the RGB itself, i.e., contamination from nontip stars became too severe. So the 0.08 mag window was the right balance of number statistics and sample purity

and also motivated by the actual measurement uncertainties. Note that all of the below analysis was also performed using a 0.05 mag window, which is the width of the F814W TRGB peak. The findings were consistent with the presented ones for a 0.08 mag window but based on exactly half the number of tip stars.

In the right panel of Figure 6, the NIRCAM JWST CMD is shown, with the tip stars marked as orange. Also plotted are the same 10 Gyr BaSTI isochrones but for the JWST/NIRCAM filters. These stars appear to form a sloped sequence along the upper edge of the RGB, which we conclude to be the TRGB. In the following section, will use these traced stars to derive a value for the color dependence of the JWST TRGB.

Note the MCR-TRGB methodology introduced in M. J. Durbin et al. (2020) provides a more rigorous approach to simultaneous determination of the multiband TRGB relation than is done here. However, its advantages can only be realized when applied to data sets with a much higher photometric signal-to-noise ratio (SNR) at the TRGB than is viable for HST to reach at the distances of the SN host galaxies like those presented in this study. It will be prudent to deploy the MCR-TRGB methodology once a sufficiently large sample of TRGB stars observed with both HST and JWST at high SNR is attained (e.g., T. Hoyt et al. 2021a; K. B. W. McQuinn et al. 2021).

4. Tip of the Red Giant Branch Measurement

In this section, we use the TRGB stars that were selected in the HST/ACS F814W band (see previous section) to estimate the slope of the IR TRGB’s magnitude–color relation as observed in the NIRCAM bands. We then expand the sample to the full JWST footprint of NGC 4536 and estimate the TRGB via rectification (rotation) of the NIRCAM CMD using the newly determined slope. Finally, we demonstrate the impact that different adopted slope values have on the TRGB measurement in terms of the morphology of the EDR, the width of the dominant discontinuity feature, and the estimated distance modulus.

4.1. Determining the Tip of the Red Giant Branch Magnitude–Color Relation

With TRGB stars identified from the $F814W_0$ versus $(F606W - F814W)_0$ CMD, they can be immediately traced to those stars for which counterparts were found in the JWST F115W and F444W photometry. We can then infer the parameters of a linear relationship between the F115W magnitudes and $(F115W - F444W)$ colors of the TRGB stars. We present multiple approaches to fitting a line to data (from ordinary least squares to orthogonal distance regression (ODR)), which differ in their treatment of uncertainties. In all cases, the colors of the tip stars are zeroed to their mean $(F115W - F444W)$ color (1.31 mag).

4.1.1. Least Squares

Three forms of least squares fits are performed: ordinary, weighted, and inverse weighted, resulting in slopes -0.50 ± 0.12 mag mag⁻¹, -0.56 ± 0.11 mag mag⁻¹, and -1.06 ± 0.18 mag mag⁻¹, respectively. The inverted least squares was a common approach in astronomy that was meant to estimate the bias that large uncertainties on the independent variable axis can introduce into weighted fits, done so by

Table 1
Tip of the Red Giant Branch Slope Determinations

Fits to JWST TRGB Data	Slope	σ_{slope}	Δy_0^a	σ_{y_0}	x_0
Ordinary Least Squares	-0.50	0.12	0.01	0.03	1.29
Weighted Least Squares	-0.56	0.11	-0.03	0.03	1.29
Inverted Least Squares ^b	-1.06	0.18	-0.01	0.04	1.36
Deming Regression ^c	-1.12	0.25	-0.01	0.04	1.32
ODR	-0.99	0.16	0.03	0.05	1.29
BaSTI-predicted Metallicity Slopes	[Fe/H]	=[-1.90, +0.06]		dex	
Age = 10 Gyr	-0.74	0.03
Age = 4 Gyr	-0.92	0.07

Notes. The preferred estimate from ODR is bolded.

^a Intercepts zeroed to the mean across all fits and reported as shifts from that mean value.

^b The slope reported here was computed as the inverse of the best-fit value inferred via regression.

^c 68% CI determined via bootstrapping. The CI was symmetric so it is quoted here as a single quantity.

simply flipping the dependent and independent axes in a weighted least squares fit. The fit results from each are printed as the first three rows of Table 1 and plotted in the left panel of Figure 7 as the dashed–dotted–dotted, dotted, and dashed–dotted–dashed lines for ordinary, weighted, and inverse weighted, respectively.

4.1.2. Deming Regression

In the 2D case, when measurement uncertainties along both axes of variation are nonzero and disproportionately sized, any perceived correlation will become elongated along the axis with larger measurement uncertainties.⁹ An attempt to correct for this “diffusion bias” is the Deming regression (W. E. Deming 1964), which uses prior information on the ratio of expected variances due to measurement errors σ_x/σ_y to mitigate biases introduced when regressing against data with nonzero measurement errors along both axes of variation.

From the Deming regression, and an assumed variance ratio of 9 we find a slope equal to -1.12 ± 0.25 mag mag⁻¹. The uncertainty intervals are estimated via bootstrapping for 10,000 iterations. This inference should provide a better comparison with theory, or with measurements of the TRGB slope made in the same bands but at higher photometric SNR, and which will more closely approach the “true” slope as the Deming regression aims to infer. The result is plotted as the dashed line in Figure 7 and is the fourth entry in Table 1.

4.1.3. Orthogonal Distance Regression

Finally, we undertake a more appropriate treatment of 2D uncertainties via ODR. ODR minimizes the orthogonal distance of each point from the best-fit line, as opposed to just the vertical distance as in ordinary regression (see, e.g., P. T. Boggs & J. E. Rogers 1990, regarding its implementation in the Fortran package ODRPACK). The resulting best-fit slope is -0.99 ± 0.16 mag mag⁻¹. This result is plotted as a solid line in Figure 7 and is the fifth entry in Table 1.

⁹ C. Spearman (1904) referred to this as “constriction” and/or “regression dilution.” The effect was independently reported by J. P. Brodie & B. F. Madore (1980) in regards to the Cepheid PLR.

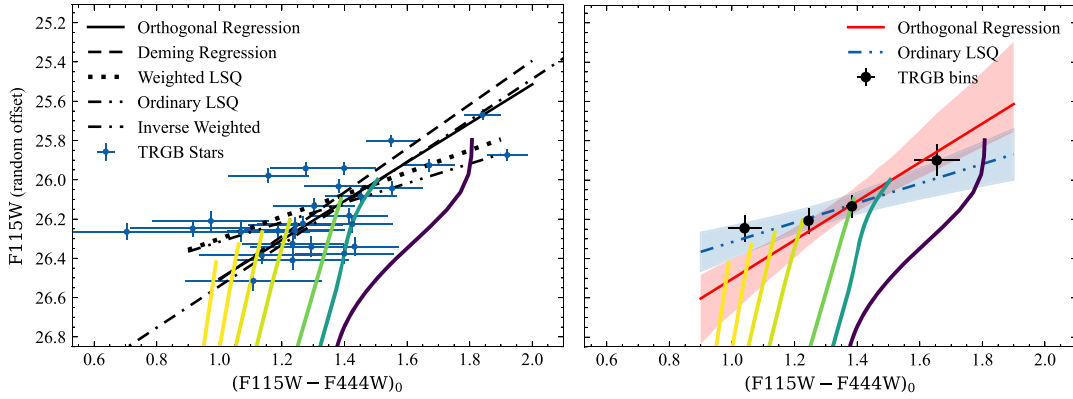


Figure 7. Fits to the TRGB’s magnitude–color relation in the F115W and F444W bandpasses. Left: F115W magnitudes vs. $(F115W - F444W)_0$ colors for tip stars (blue circles) previously shown as orange circles in Figure 6, now plotted with their photometric errors (blue lines). Note that most of the scatter about the trend lines is due to color uncertainties from the F444W magnitudes. Right: same as left panel, with four equal-number bins (sorted by color) representing the TRGB magnitudes and colors (black dots). The error bars represent the standard deviation of each quantity’s distribution within each bin. Two of the fitted lines are plotted along with their 90% confidence interval (CI) bands determined via bootstrapping: the result from ordinary least squares (blue dotted–dashed–dotted line and band) and ODR (red solid line and band). The fits were performed on the unbinned data points (left), not the binned points (right). In both panels, BaSTI 10 Gyr isochrones are again plotted on a viridis color map, this time over a metallicity range expanded to include more metal-poor isochrones, $Z = \{0.0002, 0.0004, 0.0008, 0.0014, 0.0039, 0.008, 0.017\}$ or $[\text{Fe}/\text{H}] = \{-1.90, -1.55, -1.30, -1.05, -0.60, -0.30, +0.06\}$.

4.1.4. BaSTI Isochrones

The BaSTI isochrone suite was queried and used to estimate predicted slopes in the JWST bands considered here. The isochrone metallicities are $[\text{Fe}/\text{H}] = \{-1.90, -1.55, -1.30, -1.05, -0.60, -0.30, +0.06\}$. For two set ages, 4 Gyr and 10 Gyr, the metallicity slope is then computed by fitting a line to the single brightest step at the tip of each RGB isochrone. The 10 Gyr slope is estimated to be $-0.74 \pm 0.03 \text{ mag mag}^{-1}$ and the 4 Gyr slope is $-0.92 \pm 0.07 \text{ mag mag}^{-1}$. The uncertainties are the formal standard errors returned from the fit. Their being nonzero (despite being derived from an “errorless” prediction) is a function of the discrete sampling in metallicity space, and any deviations along that discrete sampling from a dispersion-free line. In Figure 7, the 10 Gyr isochrones are plotted on a viridis color mapping. In Table 1, both slopes are presented in the last two rows. In the Appendix, the BaSTI-predicted TRGB metallicity slope is plotted from 2 Gyr to 13 Gyr in 1 Gyr steps, computed in the same way as just described.

4.2. Measuring the Tip of the Red Giant Branch in NGC 4536

In the previous sections, the region of overlap between the archival ACS/WFC and new NIRCcam imaging (hatched region outside the ellipse in Figure 1) was used to estimate the TRGB’s color dependence. In this section, we can now incorporate the remainder of the NIRCcam imaging and use the newly determined TRGB slope to “rectify” (or rotate such that the TRGB is flat in color) the CMD and measure the TRGB along the 1D magnitude axis. Simply, the F115W magnitudes are transformed as,

$$T_{115} = m_{115} - \beta(c - c_0), \quad (1)$$

where β is the adopted TRGB slope, c is a star’s color index, and c_0 is the pivot color about which the RGB is being rotated.

The area of the remaining NIRCcam data is about 1.5× larger than the subset which overlaps with HST, providing a good data set to “test” the TRGB slope that was inferred from the HST + JWST “training” data. In other words, this section demonstrates how one could use an externally calibrated TRGB slope to derive a TRGB distance in these JWST bands.

In Figure 8, a TRGB measurement is demonstrated for a rectification plus 1D edge detection approach. In the left panel, the F115W versus $(F115W - F444W)$ CMD is shown, along with the RGB color–magnitude selection, and two horizontal lines depicting the two equally likely peaks seen in the unrectified EDR (right panel, dashed transparent red lines). The F115W magnitudes are then rectified to T_{115} magnitudes with slope $\beta = -0.99 \text{ mag mag}^{-1}$ and a new RGB LF is constructed by marginalizing over color. The width of the TRGB peak in the EDR derived from the rectified LF is smaller than the separation of the two equal-strength peaks in the unrectified EDR, demonstrating the significant improvement in precision and accuracy when applying the newly determined TRGB slope to the remainder of the JWST imaging of the NGC 4536 halo.

4.3. Slope Variation Experiments

We further explore the TRGB slope with a more brute force approach to minimization. Over a grid of possible TRGB rectification slopes (from 0 to $-2.20 \text{ mag mag}^{-1}$), we recompute the EDR and document the width of the dominant edge feature (sometimes observed as a cluster of multiple, equal-power peaks). The results of this experiment are illustrated in Figure 9 and summarized in Figures 10 and 11.

In Figure 9, the EDRs as derived from seven representative sets of rectified F115W magnitudes are plotted and mapped to their unique slope values. The EDRs shown were derived from color-selected RGBs that were rotated on the CMD with corresponding slopes $\beta = \{-0.00, -0.37, -0.73, -1.10, -1.47, -1.83, -2.20\} \text{ mag mag}^{-1}$. The exact color mapping is shown in the right-hand color bar. The significant substructure in the EDR for very shallow and large values of the TRGB slope, are a result of under- or overrotation of the CMD, signaling a slope incompatible with the data. For values of the TRGB slope between about -0.7 and -1.5 , that substructure can be seen to merge into one sharp peak that approaches the minimum scale length of any feature in the EDR that can be considered real and not a noise fluctuation. This floor in the feature scale length is set by the size of the smoothing kernel, which is plotted for reference as a thick black curve in the top left

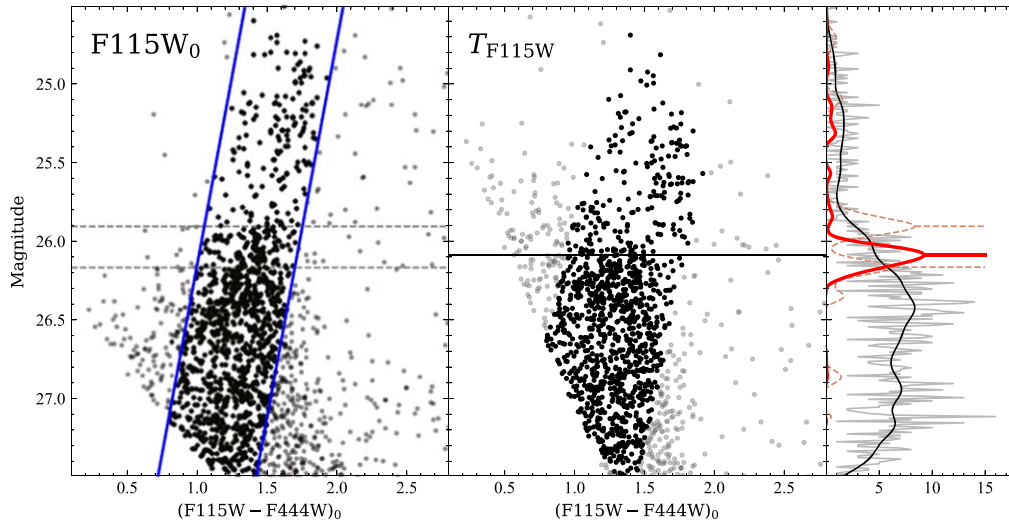


Figure 8. Demonstration of TRGB rectification in the full JWST halo data set and subsequent sharpened measurement of the IR TRGB in JWST filters. Left: F115W vs. F444W CMD. The color–magnitude selection used to select along the RGB is shown (blue lines) with RGB sources (solid black points) plotted along with non-RGB sources (transparent black points). The locations of two equally likely peaks in the resulting EDR (red dashed curves in the right-most panel) are marked (transparent, horizontal dashed lines). Middle: T_{F115W} vs. F444W CMD, wherein the stars that fall inside the unrectified RGB selection (solid black if RGB, transparent gray if not) are rotated via a separate derivation of the TRGB’s color slope (adopted here as $-0.99 \text{ mag mag}^{-1}$), such as that determined in the previous section. The resulting EDR is singly peaked, demonstrating the success of the TRGB slope in improving the clarity of the TRGB. The location of the peak magnitude is marked on the rectified CMD (horizontal black line). Right: unrectified RGB LF are computed for bins of size 0.01 mag (gray curve) and smoothed with Gaussian kernel of width 0.08 mag (black curve). Plotted also are the EDRs derived from both the unrectified (red, transparent, dashed curve) and the rectified (solid red curve) RGB magnitudes. Both EDRs have been normalized to the same peak value and scaled to the maximum value of the RGB LF. The locations of the two strong peaks in the unrectified EDR are marked (red, horizontal, dashed lines) along with the single dominant peak in the rectified EDR (red, horizontal, solid line).

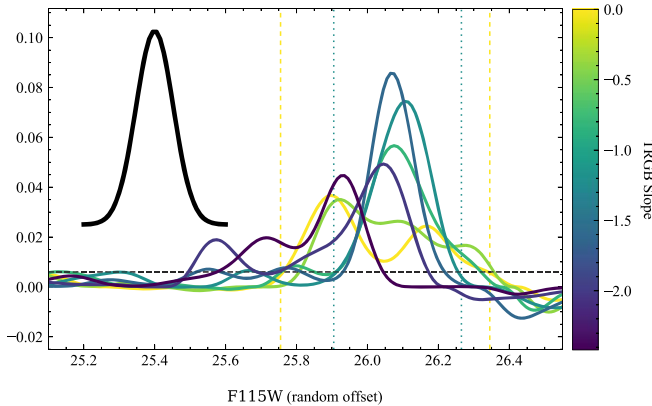


Figure 9. EDR curves computed from RGB LFs that were derived from rectified T magnitudes over a range of TRGB slopes used for the rectification. Seven representative EDRs are shown to demonstrate the behavior of vertical edge features in the rotated and color-marginalized CMD as a function of the slope used to perform said rotation. Plotted are the left and right edges of the uncorrected (slope = 0) TRGB peak as well as those belonging to the peak resulting from the ODR slope determined in the previous section (vertical dashed lines, colored to match the associated EDR curve and slope value). The threshold adopted for defining the edges of peak features is also plotted (horizontal black dashed line). For reference, the kernel used to smooth the RGB LF is shown with arbitrary height (black curve, top right).

of Figure 9. The bounds within which the peak widths were computed are also shown for two representative EDRs, one unrectified and one rectified by the best-fit value $-0.99 \text{ mag mag}^{-1}$ estimated in the previous section. The significantly reduced width of the EDR feature is a result of the merger of multiple peaks observed in the unrectified EDR into a single dominant peak.

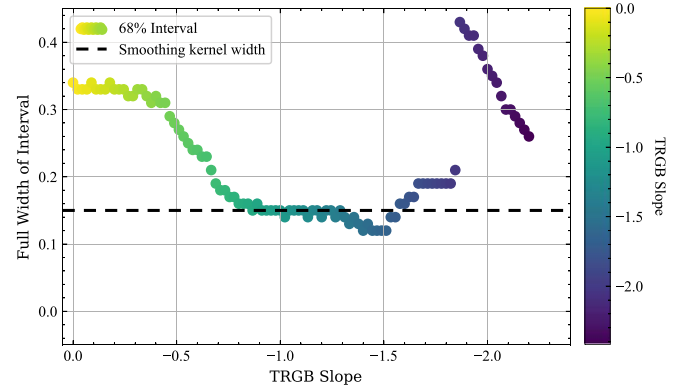


Figure 10. 68% width of the TRGB peak feature as a function of the slope that was used to flatten the TRGB feature on the CMD (rectification). One hundred linearly spaced steps in TRGB slope values ranging from -2.2 to 0.0 were considered. The width of the smoothing kernel is plotted for reference (horizontal black dashed line). Note both the x -axis and the color map are aligned to the TRGB slope axis. The redundancy is meant to aid in comparison with the representative EDRs plotted in Figure 9.

In Figure 10, this sharpening of the tip feature via rectification is shown by plotting the 68% CI widths of the TRGB peak feature as a function of adopted slope for rectification. The results show that for slope values from about -0.7 to $-1.5 \text{ mag mag}^{-1}$, the observed dispersion in the TRGB peak approaches the minimum feature size set by the size of the smoothing kernel. The results agree well with the range of slopes presented in Table 1, both the empirical estimates and BaSTI isochrone predictions.

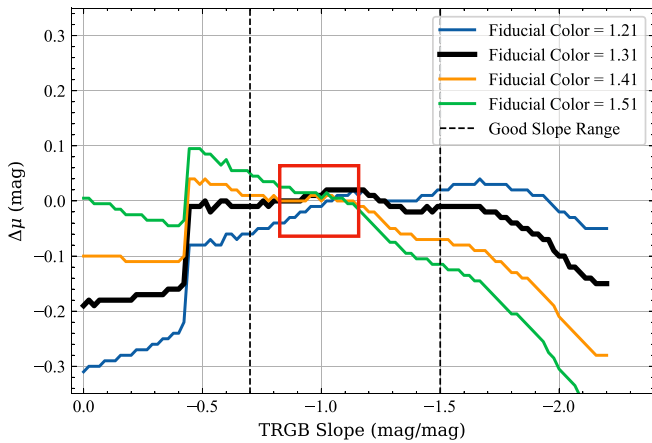


Figure 11. Delta in TRGB distance as a function of adopted TRGB slope for four fiducial calibrations. The thick, black curve represents rotation of the CMD about the mean color of the observed TRGB. The thinner, colored curves represent different pivot colors. The distance shifts $\Delta\mu$ are computed relative to the median of the black curve within the “good slope range” (vertical lines), determined from the top panel. The red, boxed region encloses the suite of curves contained by the standard error interval of the ODR results from the optical–IR trace method.

In Figure 11, the shift in the estimated TRGB distance is plotted as a function of adopted TRGB slope for four hypothetical fiducial calibrations of the TRGB. That is, β is varied continuously and c_0 is set to four fiducial values. This is meant to approximate how the TRGB distance estimated to this galaxy might change depending on both the TRGB slope and the mean color of one’s TRGB calibration data set, e.g., the color of the TRGB in geometric anchors like NGC 4258 or the LMC. The shifts in distance $\Delta\mu$ are computed relative to the median of the TRGB magnitudes within the -0.7 to -1.5 mag mag^{-1} range of “good” slope values (see top panel and previous paragraph). It can be seen that, for slope values outside the good range (including zero, i.e., no color correction), the observed bias in TRGB distance can become as large as 0.3 mag. On the other hand, for all slope values within the good range, the deviations never exceed 0.1 mag over all fiducials. This demonstrates that even a relatively weak constraint on the TRGB slope significantly decreases color-dependent biases in TRGB distance measurement.

The red boxed region in Figure 11 encloses the set of curves that lies within one standard error of the nominal ODR results for the TRGB slope in the previous section ($\beta = 0.99 \pm 0.16$ mag mag^{-1}). This provides an estimate of the additional (systematic) contribution to the TRGB distance error incurred by extrapolating a TRGB slope calibration from different fiducial colors. This is identical in concept to the additional uncertainty observed in applications of the Cepheid Leavitt Law due to an offset between the fiducial period of one’s zero-point-calibrating Cepheid sample and the target galaxy.

5. Discussion

In the above sections, the Cepheids, JAGB, and TRGB were each identified from JWST imaging of NGC 4536. The TRGB’s color dependence was then examined in closer detail through various analyses. In this section we place the TRGB slope findings in context with the literature and discuss the prospects for future TRGB measurements with JWST.

5.1. Tip of the Red Giant Branch Results from This Study

The color slope of the IR TRGB in the considered JWST bands was estimated by tracing tip stars identified in overlapping HST imaging to their crossmatched NIRCAM magnitudes, then performing various minimizations—the intent being broad coverage of different approaches to treatment of measurement uncertainties. The estimated slopes ranged from -0.50 to -1.12 mag mag^{-1} . Shallower values came from conventional least squares approaches and steeper ones from accounting for the larger uncertainties on the color axis. The ODR slope of -0.99 ± 0.16 mag mag^{-1} should ostensibly be the most accurate inference for uncertainties along both axes, given accurate measurement uncertainties and identification of TRGB stars.

Shown in Figure 8, this slope value was then used to rotate the halo-selected CMD and flatten the TRGB feature (or “rectification”). A 1D edge detection was computed from the RGB LFs constructed from each of the unrectified and rectified CMDs. The EDR computed from the unrectified RGB LF showed a clear bimodality, with each peak falling at the blue and red ends of the sloped TRGB feature. The EDR of the rectified RGB LF becomes singularly peaked, indicating most of the slant of the TRGB in the CMD was successfully removed.

The separation of the two peaks in the unrectified bimodal EDR was 0.28 mag, while the width of the rectified single-peaked EDR was 0.09 mag. K. B. W. McQuinn et al. (2019) briefly mention the F115W band in their isochrone overview paper and point out that the variation in TRGB luminosity due to metallicity and age is 0.3 and 0.09 mag, respectively. This is consistent with the hypothesis that our slope has corrected for metallicity effects in the observed TRGB, and that a sizable portion of the remaining dispersion in the slope-corrected measurement is possibly sourced by uncorrected age effects. Though the current number statistics preclude any further or more rigorous interpretation.

The impact of the color slope correction on TRGB measurement was then explored over a finer grid of rectification slope values. The results were illustrated in Figure 9 and the information condensed into the 68% width of the TRGB feature in Figure 10. The results revealed that β values in the range -0.7 to -1.5 mag mag^{-1} minimized the width of the TRGB feature, which is consistent with the slope values inferred earlier via the optical–IR trace method. It is important to note that the majority of the imaging used in these tests was *not* contained in the HST + JWST overlap region that was used to do the optical–IR tracing. See the hatched (HST + JWST) versus unhatched (JWST only) regions in Figure 1.

The width of the TRGB feature discussed in the previous paragraph can be viewed as a proxy for the statistical uncertainty, or the precision of a relative distance. The results demonstrated the improvement in this precision that is attained when applying a correction for the TRGB color slope, and that there exist a range of slope values that best maximize the statistical precision. Now we discuss the effect that the TRGB slope (and its uncertainty) would have on an absolute TRGB distance measured relative to a fiducial zero-point calibration.

In Figure 11, the running-slope experiment was reformulated to explore the measurement of an absolute distance to this (or any) target galaxy. The shift in estimated distance was plotted as a function of β and at four values of c_0 . Of course, the curve was flat when the target CMD was rotated about the mean color of the target TRGB, i.e., the fiducial was set to itself. Then, three hypothetical color fiducials were also plotted, to

demonstrate two parts of the distance uncertainty related to TRGB color slope correction: (1) the propagation of slope uncertainties into distance uncertainty, and (2) the amplification of that uncertainty as the difference between the color of the fiducial calibration relative to the target galaxy increases. As expected, and shown in Figure 11, the deviations in the estimated distance are larger for fiducial calibrations that are further offset from the color of the TRGB in the target galaxy. That is, for the same TRGB slope values, $\Delta\mu$ is larger for the curve based on a $c_0 = 1.51$ mag fiducial than it is for the one based on a $c_0 = 1.41$ mag fiducial.

We can also view this effect from a more practical perspective with some approximate calculations. The slope inferred from the ODR fit to the optical-identified tip stars was -0.99 ± 0.16 mag mag⁻¹. If one’s fiducial TRGB calibration has the same c_0 as the target galaxy, then the additional uncertainty from the slope extrapolation would be zero. However, if the fiducial color is 0.2 mag offset in c_0 , then the TRGB slope uncertainty propagated into the distance uncertainty would be equal to $0.2 \text{ mag} \times 0.16 \text{ mag mag}^{-1} = 0.032 \text{ mag}$. This uncertainty can also be visualized in Figure 11 as the vertical distance between the two points where the $c_0 = 1.51$ mag fiducial (green curve) intersects the projection of the ODR slope and error (red box).

This demonstrates that the color of one’s fiducial TRGB calibration should be as close as possible to the color of the target galaxy’s TRGB in order to minimize the slope extrapolation uncertainties. This effect is identical to the systematic error observed in applications of the Cepheid Leavitt Law when there is an offset between the mean period of one’s calibrator Cepheids and the mean period of a target galaxy’s Cepheids.

In all cases of our analysis, the slope intervals that best represented the empirical data contained the values of the TRGB’s metallicity slope predicted by the BaSTI isochrone suite for ages 4 and 10 Gyr of a TRGB population, equal to -0.74 and -0.92 mag mag⁻¹, respectively.

5.2. Literature Tip of the Red Giant Branch Slope Estimates

At the time of writing, there does not exist a detailed study of the TRGB slope in the specific JWST bands discussed here. So we discuss our results in the context of the similar ground-based J and K bands. The effective wavelengths of F115W and J are $1.15 \mu\text{m}$ and $1.24 \mu\text{m}$, respectively. For F444W and K they are $4.4 \mu\text{m}$ and $2.2 \mu\text{m}$, respectively. The bandpasses in the blue pair are separated by only 90 nm in effective wavelength, while the wavelength coverage of both the redder bandpasses is well into the Rayleigh–Jeans tail of an RGB star. This can be verified in Figure 5 of K. B. W. McQuinn et al. (2019) wherein the K , F277W, [3.6], and [4.5] bands all have the same TRGB magnitude on the Vega system. As a result, the J and K bands should provide a reasonable approximation of the F115W and F444W bands, respectively.

The slopes we have derived here, from either the optical-identification approach (i.e., Table 1) or the running-slope experiment (Figure 10), are consistent with literature determinations in these similar ground-based bandpasses. E. Valenti et al. (2004) reported for J versus $(J - K)$ a slope of -1.15 mag mag⁻¹ from a sample of globular clusters.¹⁰ B. F. Madore et al. (2018) found -0.85 ± 0.12 mag mag⁻¹ from a study based on

the Local Group galaxy IC 1613. And A. Serenelli et al. (2017) found -0.81 mag mag⁻¹ from a comprehensive study of stellar model predictions, testing variations in input physics as well as bolometric corrections, ranging from empirical measurements to theoretical atmosphere models.¹¹

5.3. Broader Discussion on Viability of the Infrared Tip of the Red Giant Branch

The viability of the IR TRGB as a precise distance indicator has been questioned at times over the last two decades, largely because of its significant color/metallicity dependence. In particular, M. Górski et al. (2016) used a TRGB calibration based on Galactic globular clusters (M. Bellazzini et al. 2001; E. Valenti et al. 2004) to estimate the distances to the Magellanic Clouds, and concluded that the TRGB was inconsistent at the 0.4 mag level, based on the discrepancy between their I and JHK estimations of the distance to each cloud. However, the authors chose to adopt spectroscopic metallicities that were derived from each cloud’s innermost stars (not necessarily old RGB stars) as representative of the metallicities of their TRGB stars. This may have led to an overestimate of the metallicity of the LMC TRGB stars of order 0.2 dex. For instance, APOGEE mapped abundances to CMD-selected RGB stars across the face of the LMC. The typical values of $[\text{Fe}/\text{H}]$ ranged from -1.0 to -0.5 dex, with a long tail toward the Fe-depleted end and a sharp truncation at the metal-rich end (D. L. Nidever et al. 2020). The metallicity of $[\text{Fe}/\text{H}] = -0.6$ dex adopted by M. Górski et al. (2016) lies near the uppermost end of the APOGEE distribution.

If we instead assume a value of -0.75 dex for the LMC TRGB stars, which is closer to the median of the APOGEE distribution, the M. Górski et al. (2016) I , J , and K distance moduli would shift from 18.29, 18.63, and 18.70 mag to 18.37, 18.59, and 18.63 mag, respectively. All the adjusted moduli are much closer to the detached eclipsing binary distance of 18.48 mag (G. Pietrzyński et al. 2019) than the original values. The fact that a simple shift to the mean metallicity would improve the distances they derived from *both* the I and the JK TRGB, which have oppositely signed metallicity slopes, provides additional confidence to this hypothesis of overestimated metallicities to TRGB stars. This view is also consistent with the discussion already covered by M. Górski et al. (2016) on their adopted spectroscopic versus RGB color-inferred metallicities. Most of the remaining disagreement is likely due to discrepancies in photometric zero-points between the E. Valenti et al. (2004) globular cluster catalogs and IR catalog of the LMC adopted by M. Górski et al. (2016).

5.4. A Unique Advantage of the Infrared Tip of the Red Giant Branch with JWST

The JWST/NIRCAM F090W filter is the bluest viable bandpass for making precise TRGB measurements at large distance.¹² As a result, any “secondary” band that is chosen to

¹⁰ The Valenti et al. calibration is presented in terms of $[\text{Fe}/\text{H}]$. For a transformation of their $[\text{Fe}/\text{H}]$ equations to the J and JK ones considered here, see T. J. Hoyt et al. (2018).

¹¹ The A. Serenelli et al. (2017) M_J versus $(J - K)$ calibration is presented as a second-order equation, but the linear term is an order of magnitude more dominant for $(J - K) > 0.90$ mag, which is about the color of SMC TRGB stars, so we propagate only the linear term here since these TRGB stars are much redder than those in the SMC.

¹² There are no advantages to using the F070W band for TRGB. From an instrument perspective, it is a less sensitive band than F090W and has an extremely undersampled point-spread function. And from the astrophysics perspective, TRGB stars are much fainter in F070W than in any other band installed on JWST/NIRCAM.

construct a CMD will always be redder than the “primary” one that was used to derive the TRGB distance. The secondary band being redder than the primary one carries with it some simple, yet immensely beneficial consequences. Contamination from AGB stars is reduced, particularly when using the F115W band as the primary band. And one is able to fully populate the RGB, unlike the red-truncated RGBs seen in optical CMDs such as in I versus $(V - I)$.

C-rich AGB stars and Extreme AGB (Ext-AGB) stars, which can contaminate the TRGB, are pulled away from the TRGB in the NIR. That is, the fact that the earlier-discussed JAGB population is identifiable on the CMD immediately reduces the odds that a TRGB measurement can be biased by the presence of an AGB population. Such misidentifications have led to significant (>0.4 mag) biases in TRGB measurements such as some of the ones presented in D. Scolnic et al. (2023).

In a similar vein, because of the TRGB’s negative slope in the IR, the detection of metal-poor TRGB stars immediately guarantees that one has a complete sample of TRGB stars. The loss of metal-rich stars is an observational selection effect imposed when the secondary color is bluer than the primary one. This was highlighted in Figure 6 in which the most metal-rich (solar metallicity) isochrone fell far off the HST optical CMD, but was fully contained in the JWST IR CMD.

In light of these points, the most ideal combinations for measuring precise and accurate TRGB distances with JWST are going to be F090W paired with F150W through F356W, or F115W paired with F200W through F356W. Note the use of F444W as done in this study is certainly possible, but just not ideal since it is the least sensitive NIRCAM bandpass. And the pairing of F115W with F150W provides too small a wavelength baseline, leading to an excessively steep TRGB slope.

5.5. Future Improvements

We anticipate a significantly better understanding of the IR TRGB slope will come with an enlarged sample of targets observed with JWST. This will lead to decreased statistical and systematic uncertainties in the measurement of TRGB distances with JWST.

The formal uncertainty on our slope determination from the optical–IR trace method is $0.16 \text{ mag mag}^{-1}$, or 16%. And from the running-slope experiment, the range of slopes that appeared to flatten what is ostensibly the TRGB feature in the CMD ranged from -0.7 to $-1.5 \text{ mag mag}^{-1}$. Improving these constraints will come as JWST continues to observe RGB populations both in our program and in others (e.g., K. B. W. McQuinn et al. 2021).

As emphasized in K. B. W. McQuinn et al. (2019), the variation in the IR colors and magnitudes of TRGB stars not captured by metallicity is caused by age. It will be important in future work to calibrate the TRGB slope over a range of RGB populations with various star formation histories, to essentially average over these second-order age variations, and to accurately place one’s IR TRGB distance scale onto a universal system that is anchored to a fiducial zero-point (e.g., NGC 4258).

Though it should be noted that environmental variations in both the TRGB’s slope and zero-point will likely be minimized when the TRGB is measured in the outer regions of galaxies. This is highlighted in the Appendix, where the TRGB’s metallicity-dependent color slope is predicted by the BaSTI

suite of stellar evolution models to be only weakly dependent on age in populations above a minimum age threshold (~ 6 Gyr according to those models).

6. Conclusions

In this study, we identified and isolated the TRGB, Cepheids, and JAGB from one set of JWST imaging. The characteristics of all three distance indicators in the observed JWST bandpasses were found to be in excellent agreement with ongoing expectations, including the slope and dispersion of the Cepheid Leavitt Law, the dispersion of the JAGB LF, and the slope of the IR TRGB.

The TRGB was then explored in greater detail, in particular its color dependence. First, TRGB stars were identified in overlapping HST imaging and their crossmatched JWST magnitudes used to estimate the TRGB slope. The TRGB slope parameter was then inferred using several different statistical techniques to account for the lower SNR of the secondary F444W photometry.

Several experiments were used to estimate the impact of the TRGB slope on uncertainties in the distance measurement. Notably, a bimodal pair of edge features in the uncorrected CMD was merged into a single discontinuity in the rectified CMD. This translated to an approximate reduction in TRGB magnitude measurement uncertainty from about 0.3 mag to a value less than 0.09 mag, demonstrating that the IR TRGB as observed in JWST bandpasses can be used as a precise distance indicator.

The IR TRGB slope estimates were consistent with predictions from the BaSTI suite of isochrones for old RGB populations, demonstrating that our understanding of the TRGB’s color variation is already off to a promising start. Future observations from this and other JWST programs will bolster the sample of TRGB stars we can use to converge on a more robust estimate of the TRGB’s color dependence and subsequently establish a precise and accurate JWST TRGB distance scale in the IR.

We have demonstrated here that three entirely independent distance indicators—Cepheid variables, the TRGB, and the carbon star LF (or JAGB)—can all be simultaneously detected and identified from imaging in just one JWST pointing. The next NASA flagship mission looks more than capable of providing us with a better understanding of potentially unknown systematic uncertainties that may still underlie the measurement of extragalactic distances and, subsequently, distance ladder determinations of the Hubble constant.

Acknowledgments

T.J.H. acknowledges Saul Perlmutter and Greg Aldering for their support of his research, as well as for feedback on this manuscript and its contents. T.J.H.’s contributions to this work were supported in part by the U.S. Department of Energy, Office of Science, Office of High Energy Physics under contract No. DE-AC02-05CH11231. We thank the Stellar Populations Early Release Science (ERS) team (PI: Weisz) and A. Dolphin for their provision of an early release version of their DOLPHOT software to do JWST/NIRCam photometry. We acknowledge the usage of the HyperLeda database (<http://leda.univ-lyon1.fr>). This research is based on observations made with the NASA/ESA Hubble and the NASA/ESA/CSA James Webb Space Telescopes obtained from the Space

Telescope Science Institute, which is operated by the Association of Universities for Research in Astronomy, Inc., under NASA contract NAS 5-26555 for HST, and under NASA contract NAS 5-03127 for JWST. These observations are associated with programs HST GO-13691 and JWST GO-1995. Data were downloaded from the Mikulski Archive for Space Telescopes (MAST) hosted by the Space Telescope Science Institute and can be accessed via [10.17909/rvxy-pt92](https://doi.org/10.17909/rvxy-pt92). We thank the University of Chicago and the Observatories of the Carnegie Institution for Science for their past and ongoing support of our long-term research into the calibration and determination of the expansion rate of the Universe. We thank the anonymous referee for their feedback and suggestions.

Facilities: JWST (NIRCam) and HST (ACS/WFC).

Software: DOLPHOT (A. E. Dolphin 2000; D. R. Weisz et al. 2024), astropy (Astropy Collaboration et al. 2013, 2018, 2022), jwst (H. Bushouse et al. 2023), Jupyter Notebook (T. Kluyver et al. 2016), and scipy (P. Virtanen et al. 2020).

Appendix

BaSTI Isochrones and Predicted Tip of the Red Giant Branch Slopes

The BaSTI database (S. L. Hidalgo et al. 2018; A. Pietrinferni et al. 2021) was queried over a grid of ages from 2000 to 13,000 Myr in 1000 Myr intervals and for metallicities $[\text{Fe}/\text{H}] = \{-1.90, -1.55, -1.30, -1.05, -0.60, -0.30, +0.06\}$. The brightest magnitude for each isochrone in the F115W band is then selected and used along with its corresponding (F115W – F444W) color to predict the TRGB color slope as a function of metallicity within each age bin. The result is shown in Figure 12, which demonstrates that the metallicity-dependent slope of the TRGB is predicted to vary less with age for RGB stars beyond a certain minimum age threshold (in this case ~ 6 Gyr).

This is promising in that we have reason to believe that by ensuring that we measure the IR TRGB in old-age populations, we can minimize the concomitant increase in dispersion

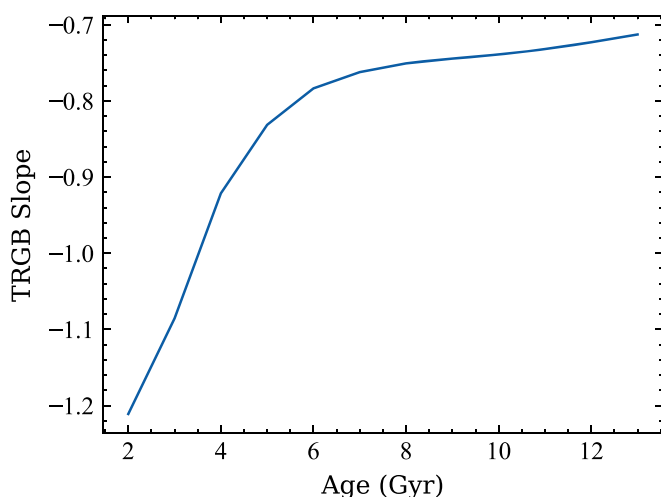


Figure 12. The TRGB’s metallicity-dependent slope determined from $[\text{Fe}/\text{H}] = -1.90$ to $+0.06$ in the F115W vs. (F115W – F444W) CMD as predicted by the BaSTI stellar evolution models for a range of ages that can be expected in galaxy stellar halos. The predicted metallicity-dependent slope decreases and the trend flattens for older populations $t_{\text{age}} \gtrsim 6$ Gyr, suggesting that targeting pristine stellar halo populations will be key to reducing population-dependent systematic errors in the measurement of TRGB distances in the IR with JWST.

necessarily incurred when transitioning TRGB measurements from the color-insensitive 800 nm to the color-dependent IR. This is imperative to emphasize in light of many recent studies that have attempted to measure the TRGB from regions of galaxies that are contaminated by young and/or intermediate-age populations (e.g., M. J. Reid et al. 2019; W. Yuan et al. 2019; G. S. Anand et al. 2022; D. Scolnic et al. 2023; J. Wu et al. 2023).

ORCID iDs

Taylor J. Hoyt <https://orcid.org/0000-0001-9664-0560>

In Sung Jang <https://orcid.org/0000-0002-2502-0070>

Wendy L. Freedman <https://orcid.org/0000-0003-3431-9135>

Barry F. Madore <https://orcid.org/0000-0002-1576-1676>

Abigail J. Lee <https://orcid.org/0000-0002-5865-0220>

Kayla A. Owens <https://orcid.org/0000-0003-3339-8820>

References

- Anand, G. S., Riess, A. G., Yuan, W., et al. 2024, *ApJ*, 966, 89
- Anand, G. S., Tully, R. B., Rizzi, L., Riess, A. G., & Yuan, W. 2022, *ApJ*, 932, 15
- Astropy Collaboration, Price-Whelan, A. M., Lim, P. L., et al. 2022, *ApJ*, 935, 167
- Astropy Collaboration, Price-Whelan, A. M., Sipőcz, B. M., et al. 2018, *AJ*, 156, 123
- Astropy Collaboration, Robitaille, T. P., Tollerud, E. J., et al. 2013, *A&A*, 558, A33
- Baade, W. 1944, *ApJ*, 100, 137
- Baade, W., & Swope, H. H. 1963, *AJ*, 68, 435
- Beaton, R. L., Seibert, M., Hatt, D., et al. 2019, *ApJ*, 885, 141
- Bellazzini, M. 2008, *MmSAI*, 79, 440
- Bellazzini, M., Ferraro, F. R., & Pancino, E. 2001, *ApJ*, 556, 635
- Bellazzini, M., Ferraro, F. R., Sollima, A., Pancino, E., & Origlia, L. 2004, *A&A*, 424, 199
- Boggs, P. T., & Rogers, J. E. 1990, *Contemporary Mathematics*, 112, 183
- Boyer, M. L., Anderson, J., Gennaro, M., et al. 2022, *RNAAS*, 6, 191
- Brodie, J. P., & Madore, B. F. 1980, *MNRAS*, 191, 841
- Bushouse, H., Eisenhamer, J., Dencheva, N., et al. 2023, JWST Calibration Pipeline, v1.9.6, Zenodo, doi:10.5281/zenodo.7038885
- de Vaucouleurs, G. 1978, *ApJ*, 223, 351
- Deming, W. E. 1964, *Statistical Adjustment of Data* (New York: Dover Publications)
- Dey, A., Schlegel, D. J., Lang, D., et al. 2019, *AJ*, 157, 168
- Dolphin, A. E. 2000, *PASP*, 112, 1383
- Durbin, M. J., Beaton, R. L., Dalcanton, J. J., Williams, B. F., & Boyer, M. L. 2020, *ApJ*, 898, 57
- Freedman, W. L. 1988, *ApJ*, 326, 691
- Freedman, W. L. 2021, *ApJ*, 919, 16
- Freedman, W. L., & Madore, B. F. 1988, *ApJL*, 332, L63
- Freedman, W. L., & Madore, B. F. 1990, *ApJ*, 365, 186
- Freedman, W. L., & Madore, B. F. 2020, *ApJ*, 899, 67
- Freedman, W. L., & Madore, B. F. 2023, *JCAP*, 2023, 050
- Freedman, W. L., Madore, B. F., Gibson, B. K., et al. 2001, *ApJ*, 553, 47
- Freedman, W. L., Madore, B. F., Hatt, D., et al. 2019, *ApJ*, 882, 34
- Freedman, W. L., Madore, B. F., Scowcroft, V., et al. 2012, *ApJ*, 758, 24
- Gardner, J. P., Mather, J. C., Abbott, R., et al. 2023, *PASP*, 135, 068001
- Górski, M., Pietrzyński, G., Gieren, W., et al. 2016, *AJ*, 151, 167
- Hamer, S. L., Ardern, S., & Scowcroft, V. 2023, arXiv:2302.14075
- Hernstein, J. R., Moran, J. M., Greenhill, L. J., et al. 1999, *Natur*, 400, 539
- Hidalgo, S. L., Pietrinferni, A., Cassisi, S., et al. 2018, *ApJ*, 856, 125
- Hoffmann, S. L., Macri, L. M., Riess, A. G., et al. 2016, *ApJ*, 830, 10
- Hoyt, T., Freedman, W. L., Beaton, R. L., et al. 2021a, A High-accuracy, Geometric Calibration of the Tip of the Red Giant Branch in the Halo of NGC 4258, HST Proposal. Cycle 29, ID. #16743
- Hoyt, T. J. 2023, *NatAs*, 7, 590
- Hoyt, T. J., Beaton, R. L., Freedman, W. L., et al. 2021b, *ApJ*, 915, 34
- Hoyt, T. J., Freedman, W. L., Madore, B. F., et al. 2018, *ApJ*, 858, 12
- Hu, W. 2005, in *ASP Conf. Ser. 339, Observing Dark Energy*, ed. S. C. Wolff & T. R. Lauer (San Francisco, CA: ASP), 215
- Hubble, E. 1929, *PNAS*, 15, 168

- Humphreys, E. M. L., Reid, M. J., Greenhill, L. J., Moran, J. M., & Argon, A. L. 2008, *ApJ*, **672**, 800
- Humphreys, E. M. L., Reid, M. J., Moran, J. M., Greenhill, L. J., & Argon, A. L. 2013, *ApJ*, **775**, 13
- Jang, I. S. 2023, *MNRAS*, **521**, 1532
- Jang, I. S., Hoyt, T. J., Beaton, R. L., et al. 2021, *ApJ*, **906**, 125
- Jang, I. S., & Lee, M. G. 2017, *AJ*, **835**, 28
- Kluyver, T., Ragan-Kelley, B., Pérez, F., et al. 2016, in *Positioning and Power in Academic Publishing: Players, Agents and Agendas*, ed. F. Loizides & B. Schmidt (Amsterdam: IOS Press), 90
- Leavitt, H. S. 1908, *AnHar*, **60**, 87
- Leavitt, H. S., & Pickering, E. C. 1912, *HarCi*, **173**, 1
- Lee, A. J., Freedman, W. L., Jang, I. S., Madore, B. F., & Owens, K. A. 2024a, *ApJ*, **961**, 132
- Lee, A. J., Freedman, W. L., Madore, B. F., et al. 2021, *ApJ*, **907**, 112
- Lee, A. J., Monson, A. J., Freedman, W. L., et al. 2024b, *ApJ*, **967**, 22L
- Lee, M. G., Freedman, W. L., & Madore, B. F. 1993, *ApJ*, **417**, 553
- Macri, L. M., Calzetti, D., Freedman, W. L., et al. 2001, *ApJ*, **549**, 721
- Macri, L. M., Ngeow, C.-C., Kanbur, S. M., Mahzooni, S., & Smitka, M. T. 2015, *AJ*, **149**, 117
- Madore, B. F., & Freedman, W. L. 2020a, *ApJ*, **899**, 66
- Madore, B. F., & Freedman, W. L. 2020b, *AJ*, **160**, 170
- Madore, B. F., Freedman, W. L., Hatt, D., et al. 2018, *ApJ*, **858**, 11
- Madore, B. F., Mager, V., & Freedman, W. L. 2009, *ApJ*, **690**, 389
- Makarov, D., Prugniel, P., Terekhova, N., Courtois, H., & Vauglin, I. 2014, *A&A*, **570**, A13
- McQuinn, K. B. W., Boyer, M., Skillman, E. D., & Dolphin, A. E. 2019, *ApJ*, **880**, 63
- McQuinn, K. B. W., Boyer, M. L., Dolphin, A. E., Newman, M. J. B., & Skillman, E. D. 2021, *Securing the TRGB Distance Indicator: A Pre-Requisite for a JWST Measurement of H₀*, JWST Proposal. Cycle 1, ID. #1638
- Monson, A. J., Freedman, W. L., Madore, B. F., et al. 2012, *ApJ*, **759**, 146
- Mould, J., & Kristian, J. 1986, *ApJ*, **305**, 591
- Nidever, D. L., Hasselquist, S., Hayes, C. R., et al. 2020, *ApJ*, **895**, 88
- Nikolaev, S., & Weinberg, M. D. 2000, *ApJ*, **542**, 804
- Owens, K. A., et al. 2024, *ApJ*, submitted
- Parada, J., Heyl, J., Richer, H., Ripoche, P., & Rousseau-Nepton, L. 2021, *MNRAS*, **501**, 933
- Parada, J., Heyl, J., Richer, H., Ripoche, P., & Rousseau-Nepton, L. 2023, *MNRAS*, **522**, 195
- Persson, S. E., Madore, B. F., Krzemiński, W., et al. 2004, *AJ*, **128**, 2239
- Pietrinferni, A., Hidalgo, S., Cassisi, S., et al. 2021, *ApJ*, **908**, 102
- Pietrzyński, G., Graczyk, D., Gallenne, A., et al. 2019, *Natur*, **567**, 200
- Reid, M. J., Pesce, D. W., & Riess, A. G. 2019, *ApJL*, **886**, L27
- Riess, A. G., Anand, G. S., Yuan, W., et al. 2024, *ApJL*, **962**, L17
- Riess, A. G., Breuval, L., Yuan, W., et al. 2022, *ApJ*, **938**, 36
- Riess, A. G., Macri, L., Casertano, S., et al. 2009, *ApJ*, **699**, 539
- Riess, A. G., Macri, L. M., Hoffmann, S. L., et al. 2016, *ApJ*, **826**, 56
- Rigby, J., Perrin, M., McElwain, M., et al. 2023, *PASP*, **135**, 048001
- Ripoche, P., Heyl, J., Parada, J., & Richer, H. 2020, *MNRAS*, **495**, 2858
- Saha, A., Sandage, A., Labhardt, L., et al. 1996, *ApJ*, **466**, 55
- Salaris, M., & Cassisi, S. 1998, *MNRAS*, **298**, 166
- Salaris, M., & Cassisi, S. 2005, *Evolution of Stars and Stellar Populations*
- Sandage, A. 1994, *Calibration of Nearby Galaxy Type IA Supernovae as Standard Candles: NGC4496 and NGC4356—CYCLE4MEDIUM*, HST Proposal ID 5427. Cycle 4
- Sandage, A. R. 1970, *PhT*, **23**, 34
- Schlafly, E. F., & Finkbeiner, D. P. 2011, *ApJ*, **737**, 103
- Schlegel, D. J., Finkbeiner, D. P., & Davis, M. 1998, *ApJ*, **500**, 525
- Scolnic, D., Riess, A. G., Wu, J., et al. 2023, *ApJL*, **954**, L31
- Scowcroft, V., Freedman, W. L., Madore, B. F., et al. 2011, *ApJ*, **743**, 76
- Scowcroft, V., Seibert, M., Freedman, W. L., et al. 2016, *MNRAS*, **459**, 1170
- Serenelli, A., Weiss, A., Cassisi, S., Salaris, M., & Pietrinferni, A. 2017, *A&A*, **606**, A33
- Spearman, C. 1904, *American Journal of Psychology*, **15**, 201
- Valenti, E., Ferraro, F. R., & Origlia, L. 2004, *MNRAS*, **354**, 815
- Virtanen, P., Gommers, R., Oliphant, T. E., et al. 2020, *NatMe*, **17**, 261
- Weinberg, M. D., & Nikolaev, S. 2001, *ApJ*, **548**, 712
- Weisz, D. R., Dolphin, A. E., Savino, A., et al. 2024, *ApJS*, **271**, 47
- Weisz, D. R., McQuinn, K. B. W., Savino, A., et al. 2023, *ApJS*, **268**, 15
- Wu, J., Scolnic, D., Riess, A. G., et al. 2023, *ApJ*, **954**, 87
- Wu, P.-F., Tully, R. B., Rizzi, L., et al. 2014, *AJ*, **148**, 7
- Yuan, W., Riess, A. G., Macri, L. M., Casertano, S., & Scolnic, D. M. 2019, *ApJ*, **886**, 61
- Zgirski, B., Pietrzyński, G., Gieren, W., et al. 2021, *ApJ*, **916**, 19